Astron. Astrophys. 315, 243–252 (1996)

ASTRONOMY AND ASTROPHYSICS

Kinematics of the galactic supernova remnants RCW 86, MSH 15-56 and MSH 11-61*A*

M. Rosado[1], P. Ambrocio-Cruz[2], E. Le Coarer[3], and M. Marcelin[2]

[1] Instituto de Astronomía, UNAM, Apdo. 70-264, México, D.F., 04510, México
[2] Observatoire de Marseille, 2, Place Le Verrier, F-13248 Marseille Cedex 4, France
[3] Observatoire de Grenoble, BP53X Grenoble Cedex, France

Received 22 September 1995 / Accepted 2 May 1996

Abstract. We have studied the kinematics of the galactic supernova remnants (SNRs) RCW 86, MSH 15-*56* and MSH 11-*61A* as the first step of a long term project of determination of kinematic distances to galactic SNRs with optical counterparts. We have obtained the kinematic distances to these nebulae. Our results on RCW 86 imply a real association between this SNR and a neighboring OB stellar association, confirming that this SNR, which is now in the Sedov phase, is probably the result of an explosion of a Type II supernova. Furthermore, we argue against the identification of RCW 86 with the historical supernova AD185. We have detected an almost complete shell of optical filaments associated with the SNR MSH 15-*56*. The large diameter derived from its kinematic distance suggests that this SNR is in the radiative phase of evolution. Finally, we estimate that the SNR MSH 11-*61A* is located at about 7 kpc from the Sun in a zone where several background and foreground nebulae at different velocities are seen in projection. Its linear diameter is 31 pc, about twice the value given by previous determinations.

Key words: ISM: supernova remnants – ISM: kinematics and dynamics – ISM: individual objects: RCW 86 – ISM: individual objects: MSH 15-*56* – ISM: individual objects: MSH 11-*61A*

1. Introduction

Supernovae (SN) explosions are one of the most important sources of energy and heavy elements of the interstellar medium (ISM) in a galaxy via the interaction of the stellar ejecta with the ISM. Those interactions give rise to the formation of supernova remnants (SNRs). In our Galaxy, there are about 180 identified SNRs of which only about 30 have optical counterparts (Green 1991, van den Bergh 1978). Much has been done on this sub-set of objects because optical data complement the studies in other wavelengths and allow us to determine the physical and chemical conditions of the SNRs. Nevertheless, optical kinematic data are still scarce.

On the other hand, in recent years, considerable effort has been made to study systematically, the kinematics of the ionized hydrogen in the Galaxy by means of a scanning Fabry-Perot (FP) interferometer surveying the Hα line. The aim of this galactic survey is to establish a new model of our Galaxy and its spiral arms based on accurate measurements (with precisions of 1-2 km s^{-1} in the radial velocities) of the velocities of near and distant HII regions (Georgelin et al. 1994).

Taking advantage of the results of this kinematic survey, we are studying galactic SNRs with optical counterparts using the same instrumentation. This will give us a homogeneous set of data on the SNRs as well as their environments. This should be important for the accurate determination of kinematic distances to these objects. Indeed, one of the aims of this project is to establish the reliability of kinematic distances of SNRs. This determination will require a large sample of data.

The present work is the first step in this project. It studies the kinematics of three southern SNRs of the sample: the SNRs RCW 86, MSH 15-*56* and MSH 11-*61A*, with the principal aim of obtaining their kinematic distances. In addition, our kinematic data on RCW 86 allowed us to derive the shell expansion velocity, pre-shock density and initial energy of the SN explosion. In the other cases, the faintness of the emission or the complicated kinematic field where the SNR is located prevented us from obtaining these quantities.

2. Observations and data reductions

Descriptions and details of the equipment used in the observations can be found in the papers by Le Coarer et al. (1992 and 1993). Here we give only some general aspects of the instrument.

It is a 36-cm diameter telescope equipped with a focal reducer, two scanning FP interferometers, a series of interference filters and a photon counting camera. Table 1 of Le Coarer et al.

Send offprint requests to: M. Rosado

(1992), gives the general characteristics of this equipment. We obtain FP data cubes similar to radio data cubes (x, y, λ) which have an angular resolution of 9″ and a field of view of 38′ (covered by the 256×256 pixels of the photon counting camera). The interferometers have free spectral ranges corresponding to 115 and 376 km s^{-1} and sampling spectral resolutions corresponding to 5 and 16 km s^{-1} at Hα, respectively. Given the fact that SNRs have violent internal motions, and, consequently, broad velocity profiles, the high spectral resolution FP interferometer is useless because of the overlapping of several interference orders. Thus these observations report only the results from the scanning FP interferometer of 16 km s^{-1} sampling resolution.

The limiting Hα surface brightness of this instrument is estimated to be :

$$S(H\alpha)_{\rm lim} = (1.1 \pm 0.3)10^{-6} \text{erg cm}^{-2} s^{-1} sr^{-1}\,, \qquad (1)$$

The observational technique and the number and types of data we obtain with this system are the same as those already described in Le Coarer et al. (1993); we use the same terminology here.

In these observations we have used an Hα filter (λ_c = 6563 Å; $\delta\lambda$ = 10 Å), more or less transparent to the night-sky emission lines such as geocoronal Hα at 6562.78 Åand OH nightglow lines at 6553.6 Åand 6568.78 Å. These lines are rather faint and can be subtracted from the velocity profiles because the large field of view of the instrument allows us to find zones "empty" of nebular emission where the night sky lines can be isolated.

Specialized software is able to obtain velocity profiles and to deconvolve complex profiles into several components. In this way we obtain the radial velocities of one or several components in the region of interest. The computed widths of the Gaussians give the velocity dispersion, σ, of that velocity component, corrected for the instrumental response function. It is possible to obtain monochromatic Hα images of the field by integrating the counts over the line profile up to a certain value (i.e., 40 % above the peak intensity).

3. Individual SNRs

In Table 1 we have quoted the systemic velocities of the SNRs under study in this work as well as the derived kinematic distances assuming that they follow a galactic circular rotation law (Brand & Blitz 1993). The V_{LSR} values considered here were calculated following the Standard Solar Motion recommended by the IAU. A correction of – 3.4 cosl^{II} was made on the LSR velocity values to account for the (small) variation of the solar motion relative to the population of objects used to evaluate it (Georgelin et al. 1994). We have adopted the recommended IAU values of Θ_0 = 220 km s^{-1} and R_0 = 8.5 kpc. For the quadrant with 270° $\leq l^{II} \leq$ 360°, the negative velocities are associated with two values of the distance; when this happens, we chose the closer value.

The fact of considering these SNRs as following a galactic rotation law implies the assumption that these SNRs are the product of Type II SN explosions, because only Population I objects have motions corresponding mainly to a circular rotation around the Galactic Center.

In the following discussion we have not compared the SNR distances with those obtained from the $\Sigma - D$ relation because the latter can be highly uncertain when applied to specific objects.

3.1. The SNR RCW 86

The filamentary emission nebula RCW 86 (Rodgers et al. 1960) was found to be coincident in position with the southwestern section of the shell radio source MSH 14–63 or G315.4–2.3 (Mills et al. 1961). This radio source was found to be nonthermal and polarized (Hill 1967). Further studies at radio wavelengths were performed by Caswell et al. (1975) and Milne & Dickel (1975). The SNR nature of this optical nebula was established by Westerlund & Mathewson (1966), who obtained a spectrum of the optical filaments showing the characteristic signatures of radiative shocks (high [SII]/ Hα and [OI]/Hα line-ratios). It was catalogued in the SNR atlas of van den Bergh et al. (1973). Spectroscopic studies were performed by Ruiz (1981), Leibowitz & Danziger (1983), Dennefeld (1986) and Long & Blair (1990). Einstein observations of this remnant have been made by Pisarski et al. (1984) and Claas et al. (1989). The radio and X-ray morphologies are well correlated showing a shell-type SNR of 42′ diameter and having a maximum of emission towards the SW. There are two sets of optical filaments, one to the North and the brighter to the SW. Our observations, reported here, refer to the SW set of filaments. The optical filaments are associated with the emission maxima of both radio and X-rays in the shell.

Several authors (Hill 1967, Clark & Stephenson 1977) have suggested that this SNR could be formed by the historical SN AD185. This suggestion has several implications: a fixed age, and an estimate of the distance < 1 kpc, among others. The latter implication is in conflict with other distance estimates obtained from a possible association with an OB stellar association located in the direction of the SNR (Westerlund 1969) and from optical extinction studies (Leibowitz & Danziger 1983) which estimate the distance to be greater than 2 kpc. Also, Huang & Moriarty-Schieven (1987) and Thorsett (1992) have questioned the association of RCW 86 with the SN AD185. Indeed, it seems that the SNR RCW 89, which contains the pulsar PSR 1509–58, is a better candidate than RCW 86 to be the remnant of the SN AD185. Our kinematic results (in particular, our estimated kinematic distance) also argue against the identification of RCW 86 with SN AD185. This can be seen in what follows because, the identification of RCW 86 with the historical SN AD185 would imply a young SNR with smaller linear dimensions than the ones we have determined.

Fig. 1 shows an Hα image of the SW filaments, obtained from our observations discussed in Sect. 2. These filaments are in the shell, rather far away from the SNR center (between 18′ and 20′). Thus, we do not expect to have an accurate determination of the expansion velocity if the shell is expanding spherically from the geometrical center for, in that case, due to

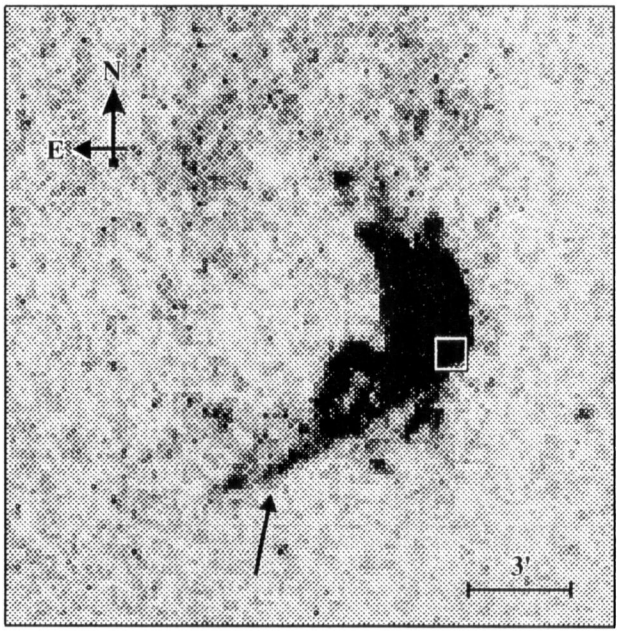

Fig. 1. Hα image of the SW filaments associated with the SNR RCW 86. The square box marks the zone where the profile shown in Fig. 3 has been extracted. The arrow shows the location of the Balmer- dominated filaments detected by Long & Blair (1990).

Table 1. Kinematic distances of the studied SNRs

Region	V_{syst} (kms^{-1})	d (kpc)	l^{II} (o)	R (pc)
RCW 86	-33.2 ± 4.5	2.8 ± 0.4	315.4	17
MSH 15-56	-58 ± 10	4.1 ± 0.7	326.3	22.2
MSH 11-61A	+12	6.9	290.1	15.5
Northern arc	-20 → -23	2.1 - 2.4	290	

NOTES:
V_{syst} - Systemic velocity of the region referred to the LSR
d - Distance to the region
R - Linear radius of the SNR,
calculated from the radio angular diameter.

Table 2. Main parameters of RCW 86 derived in this work

Linear radius of the whole shell:	17 pc
Pre-shock density of the ISM:	0.2 cm^{-3}
Pre-shock density of the dense knots:	8-10 cm^{-3}
Shock velocity of the primary blast wave:	800 km s^{-1}
Velocity of the shock induced in the knots:	110 km s^{-1}
Energy deposited in the ISM by the SN explosion:	6.6 10^{50} ergs
Age:	9.5 10^{3} yr

projection effects, the maximum velocity difference is found at the center of the remnant. On the other hand, the value of the systemic velocity, from which we obtain the kinematic distance, can be obtained from the velocities of the filaments located at the boundaries of the radio emission. Fig. 2 shows the λ-maps of the SNR emission obtained from these observations and reveals the morphology of these filaments at several velocity intervals. We detect the Balmer- dominated filaments reported by Long & Blair (1990), located to the SE of the SW filaments (marked by an arrow in Fig. 1).

To obtain the radial velocity field we have extracted velocity profiles integrated over "windows" of 5 × 5 pixels covering the region where the SNR emission is detected (the SW filaments). The extracted velocity profiles were analized by fitting one or more Gaussians once the deconvolution with the FP instrumental function is achieved. Fig. 3 shows a representative radial velocity profile of the zone marked in Fig. 1, located at the edge of the bright SW filaments. A bright component at $V_{LSR} = -33.2 \pm 4.5$ km s^{-1} is common to all the filaments. This component is quite broad and the width varies with position, reaching a maximum in the northern regions of the SW filaments (faint extensions of the crescent shaped filaments) where we measure velocity widths up to 110 km s^{-1}. In addition to this bright component, the profiles of the central region of the crescent shaped filaments show faint blue (–43 to –121 km s^{-1}) and red (+8 to +51 km s^{-1}) velocity components. We found gas (near and in the non-radiative filaments of Long & Blair 1990) with velocities up to +100 km s^{-1} but lower S/N ratios than the blue and red components already mentioned and for this reason, we did not take this gas into account in the kinematic analysis. All of these components seem to belong to the SNR gas because of their large velocities and/or widths and their morphology.

We think that the component at –33 km s^{-1} is due to gas at the systemic velocity of the SNR and that the broadening reflects the degree of violent internal motions presumably due to shocks induced by the blast wave in dense knots (Mc Kee & Cowie 1975). Another example where this happens is the SNR N120 in the LMC (Rosado et al. 1993).

The large line widths increase the uncertainty of the systemic velocity of RCW 86, implying an uncertainty of 0.4 kpc in the distance. Nevertheless, the derived kinematic distance (quoted in Table 1) supports the association of this SNR with the OB stellar association (Westerlund 1969) at 2.5 kpc.

In the case of RCW 86 there has been much controversy about the type of SN explosion which produced it, mainly because this SNR has been associated with the historical SN AD185. Our results point to a real association with the OB stellar association and, consequently, define the SN type as II. These results also support the far distance estimate (Westerlund 1969, Leibowitz & Danziger 1983).

Table 2 provides several parameters of RCW 86 obtained mainly from this work. The linear diameter was obtained from our distance estimate, the shock velocity quoted is the maximum velocity dispersion measured in the filaments and could be a lower limit. The pre-shock density was obtained from the spectroscopic observations of Leibowitz & Danziger (1983) and Ruiz (1982). These authors obtain a value of the electron density

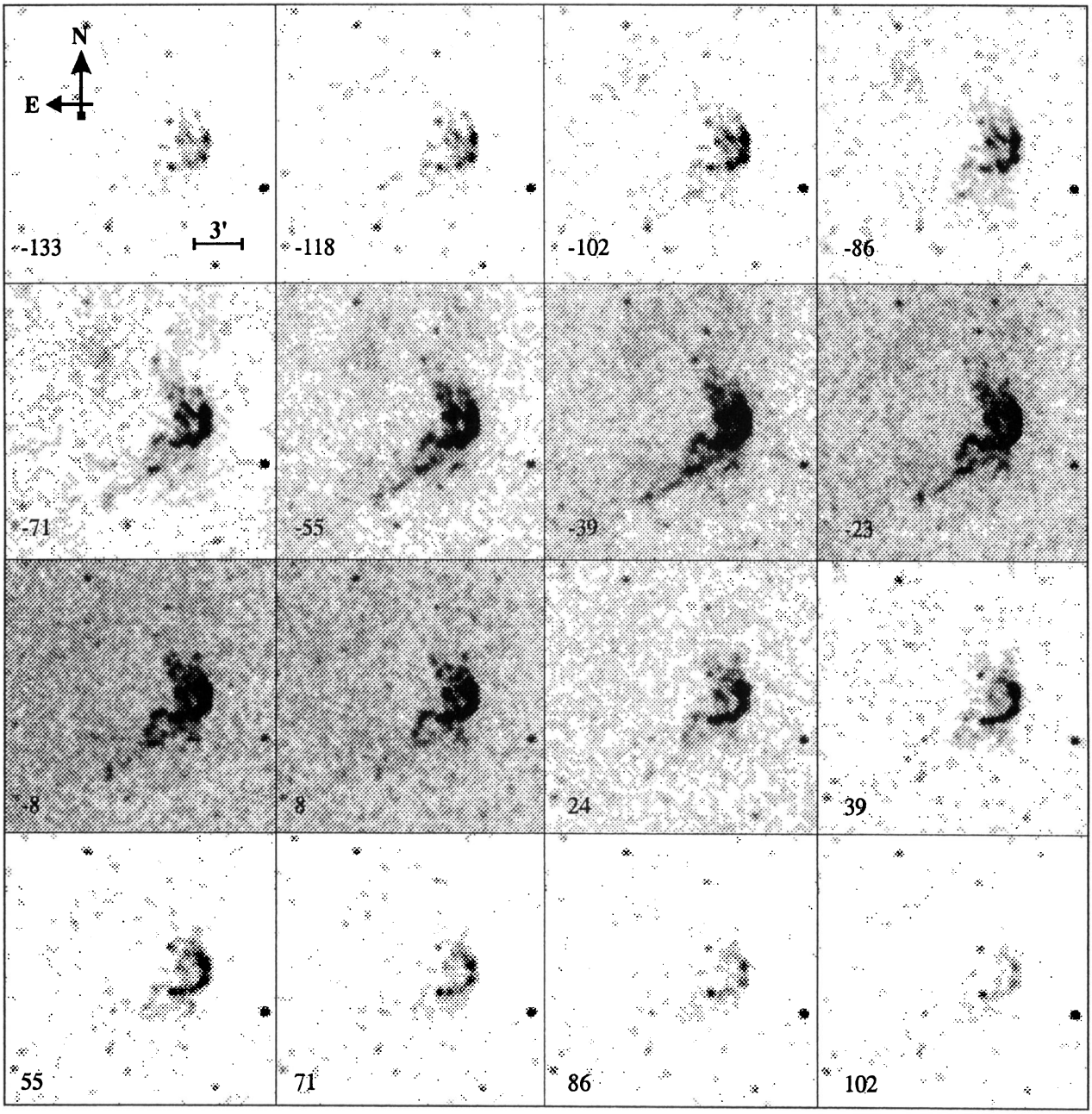

Fig. 2. λ-maps showing different velocity channels of the optical emission of the SW filaments of the SNR RCW 86 shown in Fig. 1. The LSR velocities of each channel appear, in km s^{-1}, to the bottom and to the left of each frame.

in the filaments of about 1000 cm^{-3} (based on the [SII] λ 6717 Å/λ 6731 Åline-ratio). If we consider a radiative shock compression (Spitzer 1978), then $n_e/n_o \simeq (V_{shock}/C_{sound})^2$, giving a value n_o= 8 cm^{-3} (for a value of the sound speed, C_{sound} = 10 km s^{-1}, where n_e and n_o are the post-shock and pre-shock densities and V_{shock} is the shock velocity). It is interesting to note that the line-ratios obtained in the spectroscopic works already mentioned are compatible with models of radiative shocks having n_o = 10 cm^{-3} and V_{shock} = 100 km s^{-1} (Raymond 1978, Shull & Mc Kee 1979), thus, our results on the shock velocity and pre-shock density agree quite well with the spectroscopic predictions of radiative shock models.

On the other hand, we can calculate the pre-shock density of the optical filaments if we assume that their emission is due to secondary shocks induced by a primary blast wave propagating in a medium with dense cloudlets. From Mc Kee & Cowie (1975) we know that $n_b {V_b}^2 \simeq n_c {V_c}^2$ (where n_b is the pre-shock density of the rarefied medium where the blast wave moves with a shock velocity, V_b, and n_c and V_c are the pre-shock density of the cloudlet and the shock velocity induced in the cloudlet,

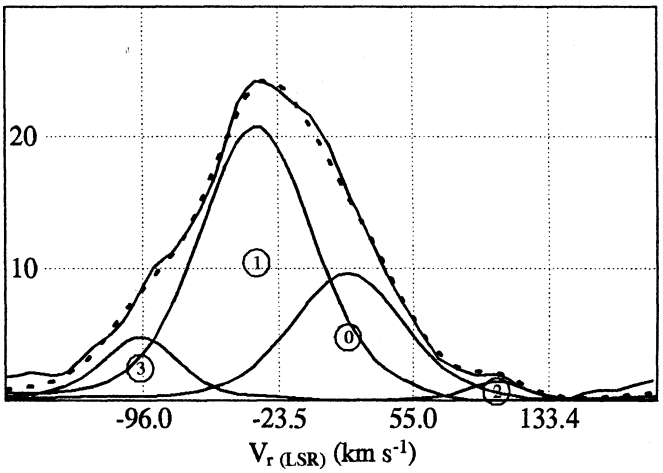

Fig. 3. Radial velocity profile integrated over the area shown in Fig. 1 of the crescent shaped filaments of RCW 86. The vertical axis is the intensity in arbitrary units. The Gaussian components which reproduce this profile are also shown (labeled from 0 to 3) as well as their addition (dashed line).

respectively; note that in this case $V_c = V_{shock}$ and $n_c = n_o$ given above).

In the case of RCW 86, the X-ray data (Claas et al. 1989) have shown that the SW region is denser than the remainder of the remnant. However, given that the shape (in radio and X-rays) is roughly spherical, it seems reasonable to assume that the blast wave has evolved in a rather uniform medium and that the SW region has only recently encountered dense and clumpy material. Thus, we will adopt a value of n_b obtained from observations in regions different than the SW one, as more indicative of the ambient pre-shock density. Consequently, we have adopted the value of $n_b = 0.2$ cm^{-3} obtained from observations of the Balmer- dominated filaments (Long & Blair 1990). This value does not depend on the distance to the remnant (whereas it is model dependent). Taking the value of $V_b = 800$ km s^{-1} for the shock velocity derived from the Balmer– dominated filaments and from the X-ray data, and using our estimated value of $V_c = 110$ km s^{-1}, we obtain $n_c = 10.5$ cm^{-3}. This agrees with our previous estimate of this quantity ($n_c = 8$ cm^{-3}) and suggests that the Mc Kee & Cowie (1975) model can explain the emission at several wavelengths. In this context, the X-ray emission is due to a shock wave moving faster in a rarefied medium, while the optical emission comes from the secondary shocks induced in the dense cloudlets.The value of the initial energy deposited in the ISM by the SN explosion derived here and quoted in Table 2 is typical of SNRs. This has been obtained under the assumption that the SNR evolution follows the Sedov model.

3.2. The SNR MSH 15-56 (G326.3 – 1.8)

This is one of the most unusual SNRs because the radio emission has a composite morphology: an internal structure extended over 10′ to the SW of the center (filled-center component like the Crab SNR), plus a well-defined shell of 36′ diameter . Clark et al. (1975) and Milne et al. (1985) found a spectral index with an abrupt change between the shell ($\alpha = -0.4$) and the internal structure ($\alpha = -0.1$ (Clark et al. 1975) or –0.04 (Milne et al. 1985)).

Previous studies have been made in order to obtain the distance to this SNR. HI absorption studies made by Caswell et al. (1975) estimate the distance to be larger than 1.5 kpc.

Fig. 4 shows an Hα image obtained from our FP interferograms as discussed in Sect. 2. In this case, before integrating the counts over the line profile to produce the monochromatic image, we performed spatial and spectral filtering of the original data cubes to smooth both spatial and spectral features. This improves the image contrast and thus we can better appreciate several optical filaments, forming an almost complete shell correlated to the 36′ diameter radio shell. We also detect some interior filaments (i.e., the ones inside the box in Fig. 4). However, we do not detect any optical counterpart to the flat spectrum radio component located near the center.

We have extracted velocity profiles of several regions covering the bright optical filaments and all of them are quite similar. Fig. 5 shows a representative radial velocity profile integrated over a window of 60 × 50 pix (marked in Fig. 4). As one can see from this figure, the contamination by night-sky emission lines (components 0 and 2 in Fig. 5) is quite strong. Indeed, the SNR component (marked as 1 in Fig. 5) has similar intensity to the night-sky lines. We found this broad SNR component in all the regions . The width of this line is variable and has a maximum value of 64 km s^{-1} toward the geometrical center of the optical shell.The intensity of this line is directly related to the morphology of the filaments. Thus we identify it with the SNR and estimated the systemic velocity as the average central value of this broad line. In Table 1 we have quoted this value as well as the kinematic distance obtained from it. Both values are somewhat uncertain because the profiles are quite broad and the emission is very faint. The Hα surface brightness for the optical filaments is about the limiting value given in Sect. 2. This value corresponds to a lower limit because it must be corrected for the interstellar absorption in that direction.

3.3. The SNR MSH 11-61A (G290.1–0.8)

An optical counterpart to this radio SNR has been found by Kirshner & Winkler (1979) and Elliott & Malin (1979). The latter authors give a contrast-enhanced [SII] photograph showing the nebulosity coincident with the radio continuum isocontours (angular diameter $\simeq 15'$). This photograph shows two features which will be important for comparison with our kinematic data: a thick filamentary feature at the northern boundary (N-filament) and a thin curved filament going from the South to the West, also at the boundaries (SW-filament). Elliott & Malin (1979) also obtained a spectrum of the southern part of the SW-filament which shows a marginally enhanced [SII]/Hα line-ratio of 0.48. This [SII]/Hα value is characteristic of stellar wind bubbles or very old SNRs (Rosado 1986). Indeed, in a log Hα/[NII] versus log Hα/[SII] diagram (Sabbadin et al. 1977), this filament is at the very limit of the zone occupied by old SNRs, almost on the

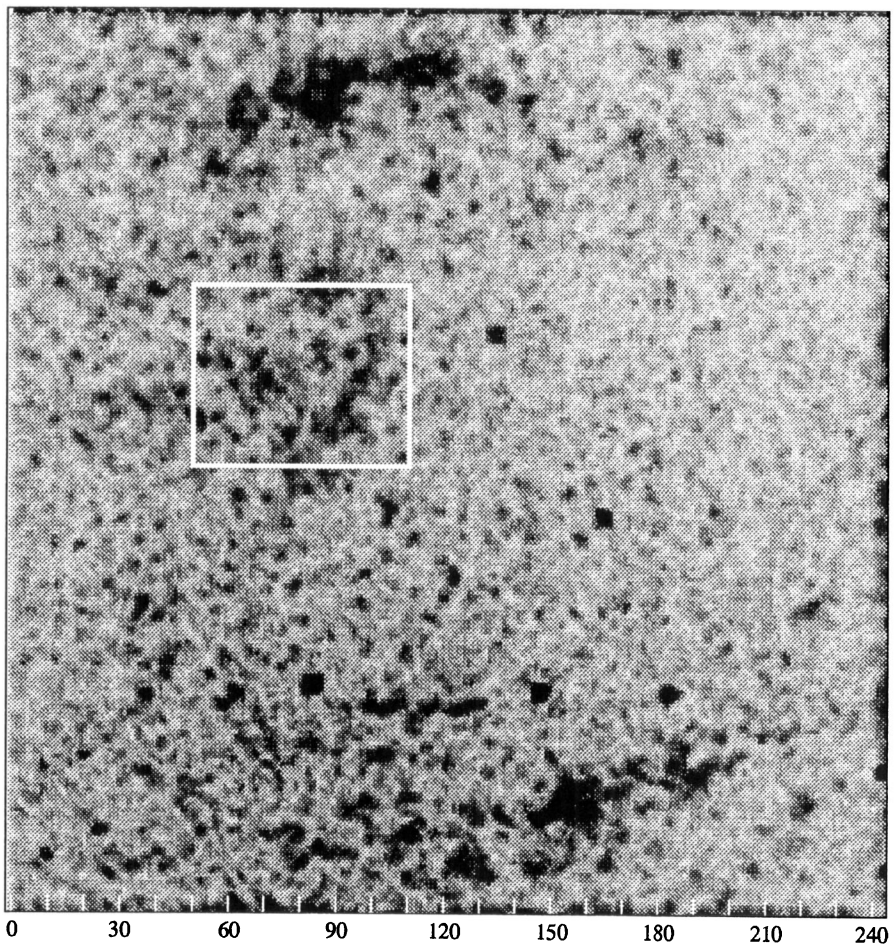

Fig. 4. Hα emission associated with the SNR MSH 15-56 revealing an almost complete filamentary shell. North is at top and East to the left. The field covers 36′. The box marks the region from which the profile shown in Fig. 5 has been extracted.

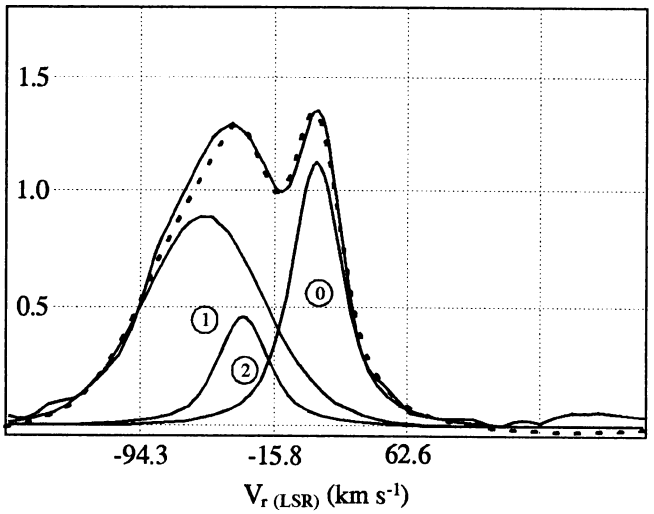

Fig. 5. Radial velocity profile, integrated over the central region shown in Fig. 4, of the SNR MSH 15-56. The Gaussian components and their addition are shown as in Fig. 3. Further discussion on these components is given in the text.

boundary with the zone occupied by HII regions. Thus, the idea of a very old (and consequently large diameter) SNR is supported. This is why Elliott & Malin (1979) assume a distance to MSH 11-61A between 12 and 14 kpc. Since there is no clear relationship between [SII]/Hα line-ratios and SNR diameters, this distance estimate is quite uncertain.

The determinations of the distance from HI absorption data (Goss et al. 1972, Dickel 1973) are based on absorption in the HI profile at LSR velocities ranging from – 20 to – 25 km s^{-1}. This velocity places the HI gas very near the tangent point ($d = R_0 \cos l^{II}$). The corrected value for the distance estimate based on HI absorption data is $\geq$ 2.9 kpc, taking the new recommended value of R_0 = 8.5 kpc. In addition, Dickel (1973) found that this SNR is located in a region where the HI background has a complicated kinematic structure consistent with a region of negative velocities to the East of the SNR, merging– in projection on the sky– into a zone of positive velocities to the West.

Our FP data at Hα allow us to study the kinematics of the whole observed field (the SNR at the center of the field, and several HII regions) by studying the morphology of the emission nebulae in several velocity slices (λ–maps) and by the extraction of velocity profiles integrated over windows of n × m pixels, over all the observed field.

Fig. 6 shows the λ-maps of the whole observed field (38′) at several LSR velocity channels and a sketch of the main features revealed in Elliott & Malin's (1979) [SII] photograph. From these, one can see how complicated the motions within the field are. There is a diffuse component at negative velocities, ex-

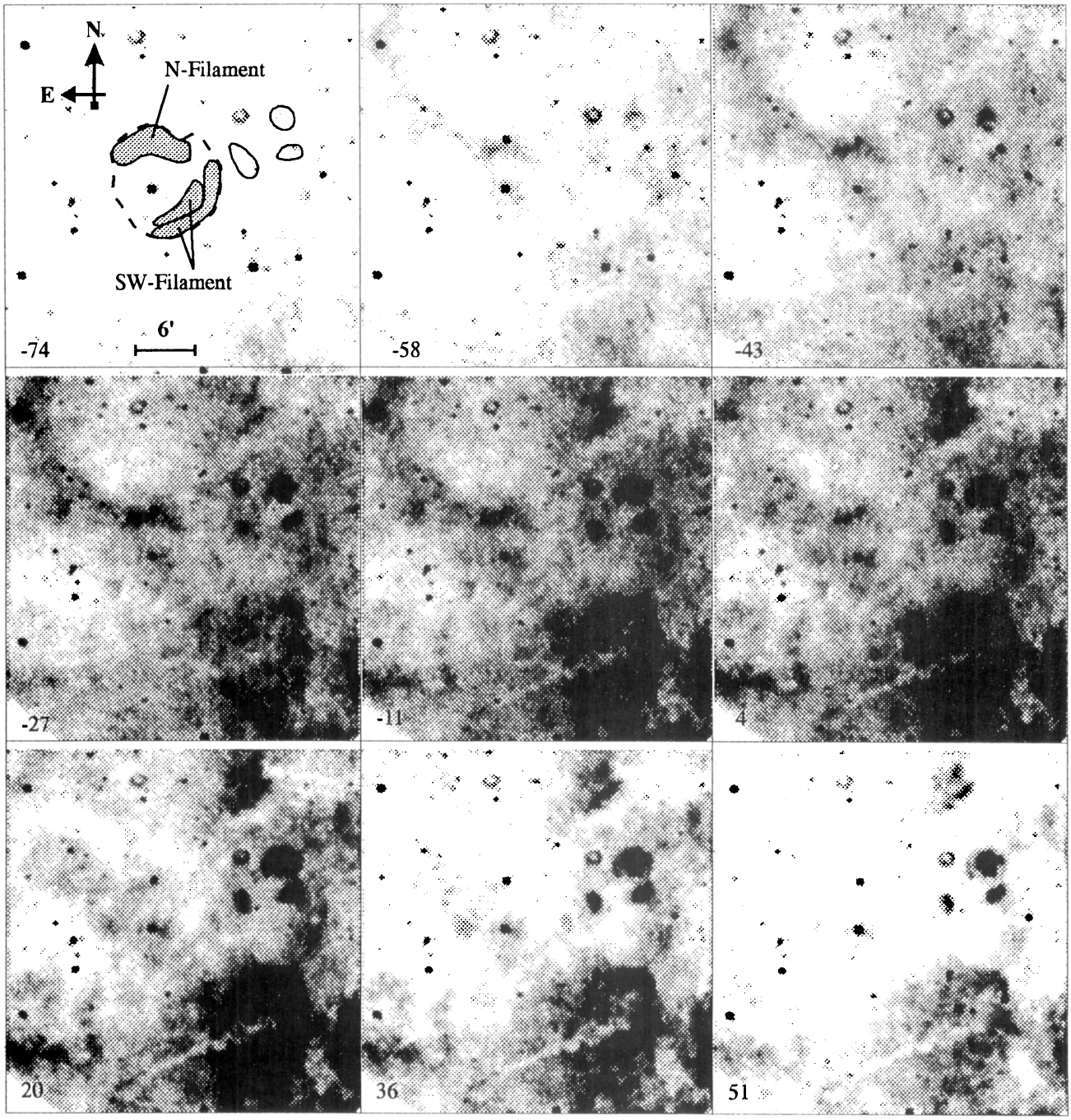

Fig. 6. λ-maps of the whole observed field (38′) containing the SNR MSH 11-61*A*. The LSR velocities of each channel appear, in km s^{-1}, to the bottom and to the left of each frame. The first frame (top left) shows a sketch, at the same scale, of the most important features revealed by Elliott & Malin's (1979) [SII] photograph.

tending over the entire field; several prominent features are also present. A large diameter arc (about 15′ radius) located in the NE quadrant of the field is detected in the channels corresponding to V_{LSR} from –58 to +20 km s^{-1} (with maximum intensity at –27 km s^{-1}). The other HII regions of the field (to the West and to the SW) are brighter at positive velocities (up to V_{LSR} = +51 km s^{-1}). This is in agreement with the complicated HI kinematics discussed by Dickel (1973). The SNR is located in a zone where both velocity components are present. Indeed, we see emission in several velocity channels with both positive and negative values. The morphology of this emission is different in each channel, however. The N-filament seen in Elliott & Malin's (1979) photograph is detected at negative velocities where it seems to belong to the large diameter arc located towards the

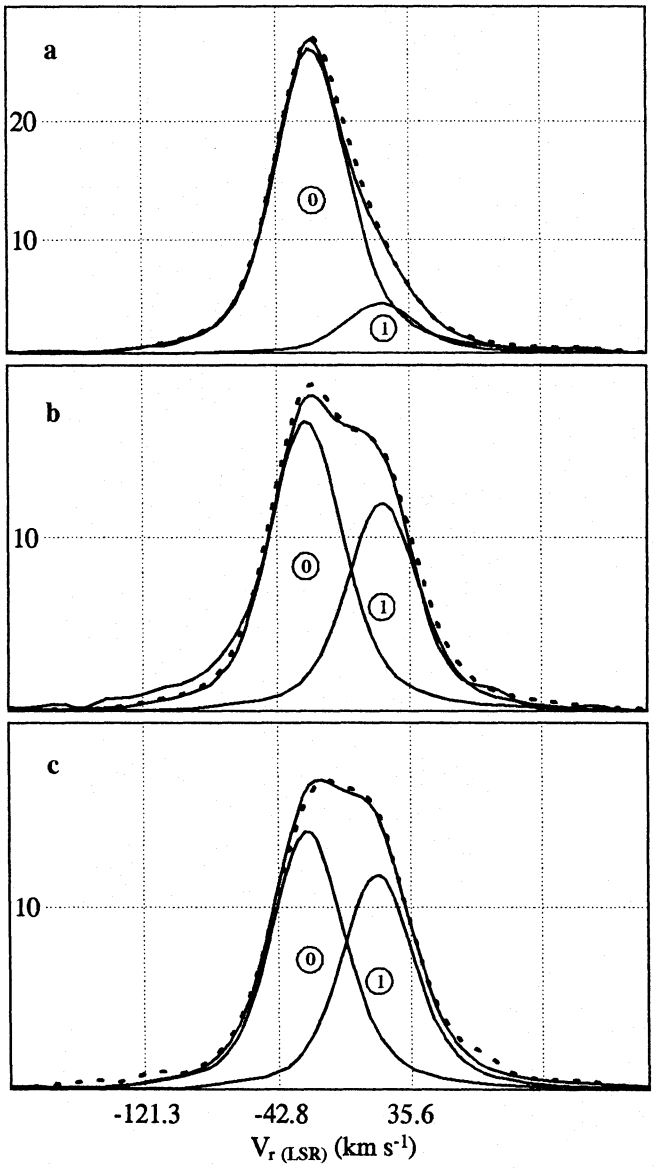

Fig. 7. Radial velocity profiles of selected regions of the SNR MSH 11-61A. a) N-filament, b) central region and c) SW-filament. The Gaussian components and their addition are shown as in Fig. 3.

NE of the field. This structure suggests that most of this emission is due to the arc and that the SNR contributes only a small amount.

To gain more insight on the kinematics of the whole observed field, we have obtained the radial velocity field of the SNR zone and neighboring areas. We have extracted velocity profiles integrated over "windows" of 20 × 20 pixels covering the whole SNR as well as neighboring HII regions. We have fitted Gaussians to these velocity profiles in a similar way as for RCW 86 (Sect. 3.1). We obtain good fits to the SNR and HII region profiles using two velocity components; good fits with a single Gaussian cannot be obtained. We find a negative velocity component (V_{LSR} from –20 to –28 km s^{-1}) and a positive velocity component with V_{LSR} from +18 to +21 km s^{-1} over all the field except at the boundaries of the SNR, where the velocity decreases slightly (to between +9 to +15 km s^{-1}). Even zones having only negative velocity emission in the λ-maps also have a faint positive component when the velocity profiles are extracted and fitted with Gaussians. Our interpretation is that we are seeing two sets of HII regions, superimposed in projection, and lying at different distances from the Sun. We detect HII regions at –20 km s^{-1}, corroborating the HI absorption measurements and implying distances at the tangent point (d ≃ 2.9 kpc), and another set of HII regions at + 20 km s^{-1}, implying distances R ≥ R_0 (d ≃ 8 kpc). Thus we are seeing, in projection, two different regions of a spiral arm.

As we have established before, in the case of the SNR zone the profiles show a composite nature. Fig. 7 shows representative radial velocity profiles at different locations: the N-filament, the center and the SW-filament of the SNR. We detect both positive and negative velocity components, and both are relatively narrow (FWHM = 30 km s^{-1}). In general, both components have the same intensity except at the N-filament, where the negative velocity component is contaminated by the bright emission of the large arc. The negative component appears very uniform in velocity over all the SNR zone. The positive velocity component, however, shows a decrease, from +20 km s^{-1} (the constant value found over the entire observed field) to +12.2 ± 2.1 km s^{-1} (average value) at the SNR boundaries. If we plot V_{LSR} as a function of distance from the geometrical center of the SNR, we find that points corresponding to negative velocities fall in a horizontal line (V_{LSR}= –23 km s^{-1}), with very little dispersion, while points corresponding to positive velocities fall in a horizontal line (V_{LSR}= +15 km s^{-1}) with more dispersion, due to the decrease in velocity at the SNR boundaries. Thus the difference in component velocities is constant with distance from the center of the SNR and, consequently, no clear indication of spherical expansion has been found. We think that this plot does not reflect the internal motions of the SNR, but only the complicated kinematics of the entire field in that l^{II} direction (unless we are in the unfortunate case of having some kind of expansion, with a strange geometry that splits the velocity profiles even at the boundaries of the SNR and gives just the same values of the velocity components detected over all the observed field). There is only a hint that the component at +12 km s^{-1} can belong to the SNR: this velocity value is found only at the boundaries of the SNR.

To check for this possibility, we subtracted, over all the field, two uniform intensity velocity components at V_{LSR}= –23 and +20 km s^{-1} of uniform intensity and then reconstructed the λ-maps. This is equivalent to a subtraction of background and foreground emission if our assumption that these components do not belong to the SNR is valid. Fig. 8 shows the reconstructed λ-maps for the SNR zone. As one can see from the figure, in the channel 1 map (corresponding to the slice of velocities: V_{LSR} = +4 ± 8 km s^{-1}) we recover the morphology seen in the [SII] photograph of Elliott & Malin (1979). The maps corresponding to other velocity channels also show emission, but either weaker or with a different morphology than the one revealed in the [SII] photograph. This confirms that the component at V_{LSR} = +12

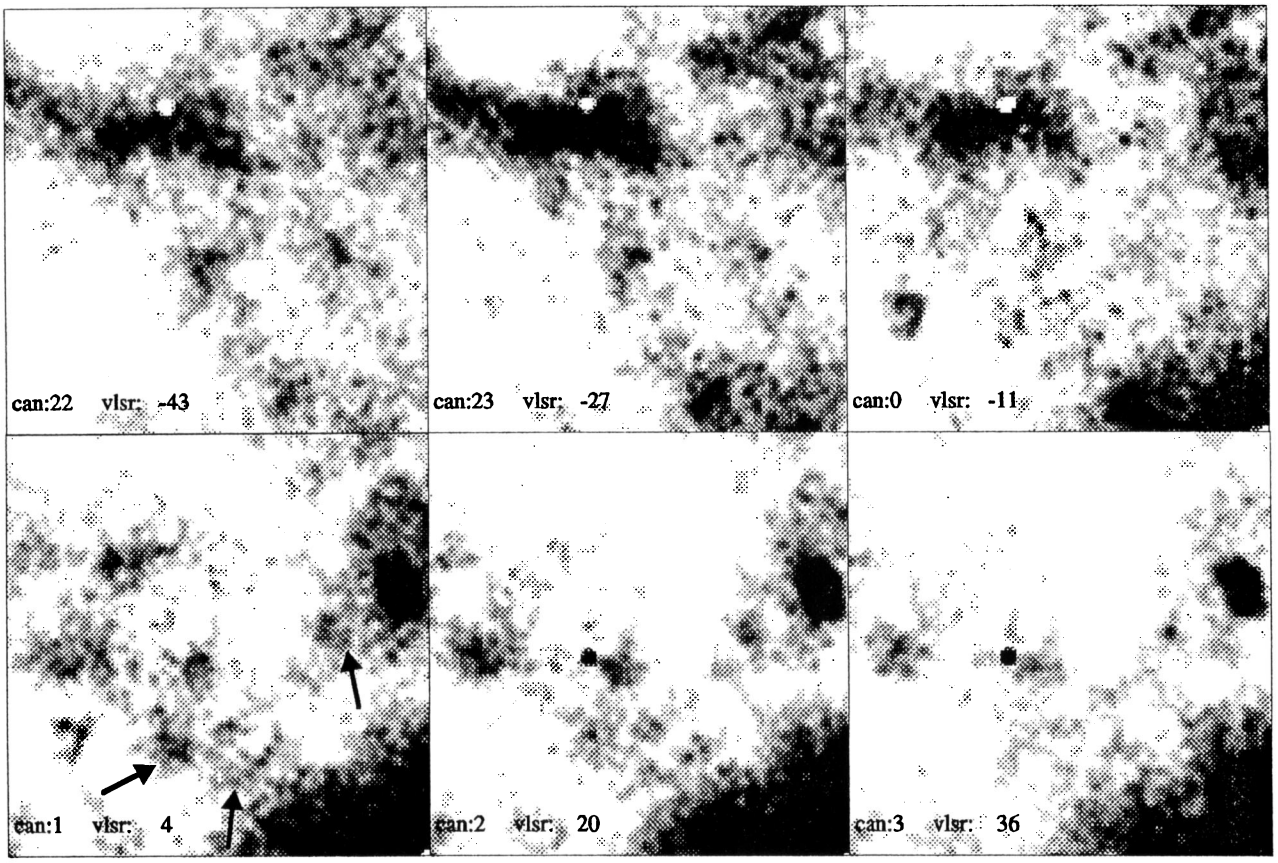

Fig. 8. λ-maps of the SNR MSH 11-61A after subtracting two uniform components at positive and negative velocities (see the text). In the channel 1 map, the SW-filament is marked by arrows. The field covers $16'.5 \times 16'.5$. North is at the top and East to the left.

km s^{-1} belongs to the SNR. We suggest that this component is at the systemic velocity of the SNR. Other arguments in favor of this choice are:

– The fact that HI absorption is found at the velocity of the tangent point, implying that the SNR is located beyond that point ($d \geq 2.9$ kpc).

– The marginal values of the [SII]/Hα line-ratio of the SW-filament, implying a SNR of large dimensions and thus relatively old.

To determine the kinematic distance to this SNR, we have adopted the positive velocity component of the SW filament as the systemic velocity of the SNR. We obtain $V_{LSR} = +12$ km s^{-1} and thus a distance of 6.9 kpc. This gives a linear radius of 15.5 pc as reported in Table 1. However, given the complexity of the Hα emission in the line of sight to this SNR, we cannot discard the negative velocity component as being part of the SNR emission. High dispersion spectroscopy in the [SII] line is required to estimate the [SII]/Hα line-ratio of each velocity component. This would help to disentangle the SNR emission from the emission of foreground or background nebulae.

4. Conclusions

In this work we have studied the kinematics of the galactic SNRs RCW 86, MSH 15-56 and MSH 11-61A.

1. From these studies we have obtained their kinematic distances.

2. In the case of RCW 86, this estimate corroborates the association of this SNR with an OB stellar association (Westerlund 1969) and rejects the identification of this SNR as the remnant of the historical SN AD185. The kinematics obtained from this work imply a more distant SNR. It was probably formed by the explosion of a Type II SN and is now in the Sedov phase of evolution. Furthermore, the broadening of the profiles allowed us to determine the velocity of the shock in the optical filaments as reported in Table 2.

3. We obtained broad velocity-profiles of the optical filamentary shell associated with the radio SNR MSH 15-56. This shell is located at the boundaries of the radio shell and is well-correlated with the radio emission. No optical counterpart has been found for the flat spectrum internal radio source. It would be interesting to try to detect such a counterpart by obtaining images with a red continuum filter. Our distance estimate implies a large diameter for this SNR which would be in its radiative phase of evolution.

4. Finally, we studied the kinematics of the SNR MSH 11-61A. The N-filament is morphologically associated with a large convex arc and does not seem to be associated with the SNR. The kinematic distance determined in this work places this SNR at

twice the distance previously estimated. However, observations in the [SII](λ 6717 Å) line are required to confirm this result.

Acknowledgements. The authors wish to acknowledge the support of the Mairie de Marseille during this work. They also thank Stan Kurtz for his comments and Alberto García for his help with the drawings.

References

Brand, J., Blitz, L. 1993, A&A, 275, 67
Caswell, J.L., Murray, J.D., Roger, R.S., et al. 1975, A&A, 45, 239
Claas, J.J., Smith, H., Kaastra, J.S.J., et al. 1989, ApJ, 337, 399
Clark, D.H., Green, A.J., Caswell, J.L. 1975, Aust.J.Phys.Astrophys.Suppl., 37, 75
Clark, D.H., Stephenson, F.R. 1977, The Historical Supernovae (Elmsford, N.Y., Pergamon), pp 83
Dennefeld, M. 1986, PASP, 92, 603
Dickel, J.R. 1973, Astrophysical Lett., 15, 61
Elliott, K.H., Malin, D.F. 1979, MNRAS 186, 45p
Georgelin, Y.M., Amram, P., Georgelin, Y.P., Le Coarer, E., Marcelin, M. 1994, A&AS, 108, 513
Goss, W.M., Radhakrishnan, V., Brooks, J.W., Murray, J.D. 1972, ApJS, 24, 123
Green, D.A. 1991, PASP, 103, 209
Hill, E.R. 1967, Aust.J.Phys., 20, 297
Huang, Y.L. Moriarty–Schieven, G.H. 1987, Science, 235, 59
Kirshner, R.P., Winkler, P.F. 1979, ApJ, 227, 853
Le Coarer, E., Amram, P., Boulesteix, J. et al. 1992, A&A, 257, 389
Le Coarer, E., Rosado, M., Georgelin, Y.P., Viale, A., Goldes, G. 1993, A&A, 280, 365
Leibowitz, E.M., Danziger, I.J. 1983, MNRAS, 204, 273
Long, K.S., Blair, W.P. 1990, ApJ, 358, L13
Mc Kee, C.F., Cowie, L.L. 1975, ApJ, 195, 715
Mills, B.Y., Slee, O.B., Hill, E.R. 1961, Aust.J.Phys., 14, 497
Milne, D.K., Dickel, J.R. 1975, Aust.J.Phys., 28, 209
Milne, D.K., Caswell, J.L., Haynes, R.F., Kesteven, M.J., Wellington, K.J., Roger, R.S., Bunton, J.D. 1985, Proc. ASAu, 6, 78
Pisarski, R.L., Helfand, D.J., Kahn, S.M. 1984, ApJ, 277, 710
Raymond, J., 1978, ApJS, 39, 1
Rodgers, A.N., Campbell, C.J., Whiteoak, J.B. 1960, MNRAS, 121, 103
Rosado, M. 1986, A&A, 160, 211
Rosado, M., Laval, A., Le Coarer, E. et al. 1993, A&A, 272, 541
Ruiz, M.T. 1981, ApJ, 243, 814
Sabbadin, F., Minello, S., Bianchini, A. 1977 A&A, 60, 147
Shull, J., Mc Kee, C. 1979, ApJ, 227, 131
Spitzer, L. 1978, Physical Processes in the Interstellar Medium (Wiley-Interscience)
Thorsett, S.E. 1992, Nature, 356, 690
van den Bergh, S., Marscher, A.P., Terzian, Y. 1973, ApJS, 26, 19
van den Bergh, S. 1978, ApJS, 38, 119
Westerlund, B.E. 1969, AJ, 74, 879
Westerlund, B.E., Mathewson, D.S. 1966, MNRAS, 131, 371

This article was processed by the author using Springer-Verlag LaTeX A&A style file version 3.